

Empirical Fourier Decomposition: An Accurate Adaptive Signal Decomposition Method

Wei Zhou^{a,b}, Zhongren Feng^{a,c}, Y.F. Xu^{b,*}, Xiongjiang Wang^a, Hao Lv^a

^a*School of Civil Engineering and Architecture, Wuhan University of Technology, Wuhan 430070, P.R. China*

^b*Department of Mechanical and Materials Engineering, University of Cincinnati, Cincinnati, OH 45221, USA*

^c*School of Urban Construction, Wuchang Shouyi University, Wuhan 430064, P.R. China*

Abstract

Signal decomposition is an effective tool to assist the identification of modal information in time-domain signals. Two signal decomposition methods, including the empirical wavelet transform (EWT) and Fourier decomposition method (FDM), have been developed based on Fourier theory. However, the EWT can suffer from a mode mixing problem for signals with closely-spaced modes and decomposition results by FDM can suffer from an inconsistency problem. An accurate adaptive signal decomposition method, called the empirical Fourier decomposition (EFD), is proposed to solve the problems in this work. The proposed EFD combines the uses of an improved frequency spectrum segmentation technique and an ideal filter bank. The segmentation technique can solve the inconsistency problem by predefining the number of modes in a signal to be decomposed and filter functions in the ideal filter bank have no transition phases, which can solve the mode mixing problem. Numerical investigations are conducted to study the accuracy of the EFD.

*Corresponding author. Tel: +1-513-556-2755.

Email addresses: weizhou@mail.uc.edu (Wei Zhou), fengz515@163.com (Zhongren Feng), xu2yf@uc.edu (Y.F. Xu), wangxiongjiang@whut.edu.cn (Xiongjiang Wang), liberty.hunter@whut.edu.cn (Hao Lv)

It is shown that the EFD can yield accurate and consistent decomposition results for signals with multiple non-stationary modes and those with closely-spaced modes, compared with decomposition results by the EWT, FDM, variational mode decomposition and empirical mode decomposition. It is also shown that the EFD can yield accurate time-frequency representation results and it has the highest computational efficiency among the compared methods.

Keywords: signal decomposition; empirical Fourier decomposition; empirical wavelet transform; Fourier decomposition method; ideal filter bank

1. Introduction

Signal decomposition is a widely used numerical tool in different fields, such as biomedical signal analysis [1], seismic signal analysis [2], mechanical vibration signal analysis [3, 4], and speech enhancement [5]. Time-domain
5 signals that derive from a physical system usually comprise several superposed components, which are referred to as modes [6], and the modes can encompass meaningful frequency-domain information of the signals, i.e. modal information. Hence, it is crucial to obtain signal decomposition results with high accuracy and efficiency.

10 In the past few decades, several signal decomposition methods have been developed, and the empirical mode decomposition (EMD)[7] is one of the most significant methods, even though its mathematical understanding is limited and it has some known shortcomings, such as robustness of mode mixing [8] and end effects [9]. Improved versions of the EMD have been
15 developed to overcome the shortcomings. The ensemble EMD [10] has been developed by adding white noise with finite amplitudes to alleviate the mode

mixing and end effects problems. The complete ensemble EMD [11] was developed to further improve the EMD by adding completeness and a full data-driven number of modes, which are missing in the ensemble EMD. Li et al. presented a time-varying filter technique to solve the mode mixing problem [12]. However, these EMD methods cannot fundamentally solve the mode mixing and end effects problems. The variational mode decomposition (VMD) [13] is a non-recursive signal decomposition method, which was developed based on a generalization of Wiener filters. However, the VMD can fail for non-stationary time-domain signals with chirp modes that have overlapping frequency ranges. To avoid this potential failure, McNeill [14] proposed the use of an optimized objective function with constraints on short-time narrow-band modes, and Chen et al. [15] exploited a complete variational framework to generalize the VMD. The empirical wavelet transform (EWT) employs an adaptive wavelet filter bank based on segments of Fourier spectra [16]. The workability of the EWT has been improved in Refs. [17, 18, 19] to eliminate its requirement for a high signal-to-noise ratio in a signal to be decomposed. However, transition phases between filter functions in a wavelet filter bank in the EWT can lead to the mode mixing problem for signals with closely-spaced modes. Besides, the first decomposed mode by the EWT can correspond to a trivial residual, with which the number of segments is not equal to that of decomposed modes. Fourier decomposition method (FDM) [20] is an adaptive non-stationary, non-linear signal decomposition method that can decompose a zero-mean signal into a set of Fourier intrinsic band functions (FIBFs) based on Fourier theory and Hilbert transform. Several limitations of the FDM have been identified. To obtain a FIBF, two frequency scan techniques were developed. One is called the low-to-high (LTH) technique and the other is high-to-low (HTL)

technique. The LTH and HTL techniques recursively estimate upper and
45 lower bounds of FIBFs, respectively. However, decomposition results by the
FDM with the two frequency scan techniques, i.e., FDM-HTL and FDM-
LTH, can be inconsistent and one cannot determine which decomposition
results are correct. Further, the two frequency scan techniques are both
iterative and can require long computation times for FDM.

50 In this work, the EWT and the FDM are briefly reviewed: the segmentation
technique and construction of a wavelet filter bank in the EWT are described,
and the construction of FIBFs and the two frequency scan techniques of
the FDM are described. A new adaptive signal decomposition method,
called the empirical Fourier decomposition (EFD), is proposed to solve the
55 aforementioned problems of the EWT and FDM. The EFD combines an
improved segmentation technique and an ideal filter bank [21]. The improved
segmentation technique has an adaptive sorting process to yield segmentation
results that are less adversely affected by noise and contains meaningful
modal information, and the ideal filter bank, whose filter functions have no
60 transition phases, facilitates accurate decomposition for signals with closely-
spaced modes. Numerical investigations are conducted to study the accuracy
of decomposition results by the EFD for two non-stationary signals and two
signals with closely-spaced modes by comparing with decomposition results
by the EMD, VMD, EWT and FDM. In addition, the accuracy of time-
65 frequency representations (TFRs) and computational efficiency of the EFD
are compared with those associated with the other methods.

The remnant of the paper is arranged as follows. In Section 2, the EWT
and FDM are briefly reviewed. In Section 3, the proposed EFD is described.
In Section 4, the numerical investigations are presented. Conclusions and
70 some discussions on future works are presented in Section 5.

2. Reviews of EWT and FDM

2.1. EWT

The EWT employs an adaptive wavelet transform algorithm based on segments of Fourier spectra [16]. The two most important steps of the EWT are: (1) use of an adaptive segmentation technique to divide Fourier spectrum of a signal to be decomposed and (2) construction of a wavelet filter bank [22]. Assume that the spectrum is defined on a normalized frequency range $[-\pi, \pi]$. The segmentation technique and wavelet filter bank for the spectrum in the frequency range $[0, \pi]$ are described below, and those for the spectrum in the frequency range $[-\pi, 0]$ can be deduced based on Hermitian symmetry of Fourier spectrum in the normalized frequency range $[-\pi, \pi]$.

One segmentation technique for the EWT is the local maxima technique [16], in which the spectrum in $[0, \pi]$ is divided into N contiguous frequency segments. Each segment is denoted by $S_n = [\omega_{n-1}, \omega_n]$ with $n \in [1, N]$, $\omega_0 = 0$ and $\omega_N = \pi$. To determine values of ω_n , the first $N - 1$ largest local maxima of the spectrum magnitude are identified. The frequencies that uniquely correspond to the identified maxima are re-indexed in descending order and denoted by $[\Omega_1, \Omega_2, \dots, \Omega_{N-1}]$ such that $\Omega_1 < \Omega_2 < \dots < \Omega_{N-1}$; in addition, $\Omega_0 = 0$ is defined. The value of ω_n is expressed by

$$\omega_n = \frac{\Omega_{n-1} + \Omega_n}{2}, n \in [1, N - 1] \quad (1)$$

which concludes the local maxima technique. As an alternative to the local maxima technique, the lowest minima technique [23] was developed for the EWT: the spectrum division and frequency reindexing procedures, which are the same as those in the local maxima technique, are first carried out. Then the minimum of the spectrum magnitude in the frequency range $[\Omega_{n-1}, \Omega_n]$

95 is identified and the value of ω_n is determined by

$$\omega_n = \arg \min_{\omega} X_n(\omega) \quad (2)$$

where $X_n(\omega)$ denotes spectrum magnitudes between in $[\Omega_{n-1}, \Omega_n]$ and $\arg \min(\cdot)$ denotes argument of the minimum, respectively, which concludes the lowest minima technique.

The wavelet filter bank is then constructed, and it consists of an empirical
100 scaling function $\hat{\phi}_1(\omega)$ and a series of empirical wavelet functions $\hat{\psi}_n(\omega)$, which are expressed by

$$\hat{\phi}_1(\omega) = \begin{cases} 1 & \text{if } |\omega| \leq \omega_1 - \tau_1 \\ \cos \left[\frac{\pi}{2} \beta \left(\frac{1}{2\tau_1} (\tau_1 + |\omega| - \omega_1) \right) \right] & \text{if } \omega_1 - \tau_1 \leq |\omega| \leq \omega_1 + \tau_1 \\ 0 & \text{otherwise} \end{cases} \quad (3)$$

and

$$\psi_n(\omega) = \begin{cases} 1 & \text{if } \omega_n + \tau_n \leq |\omega| \leq \omega_{n+1} - \tau_{n+1} \\ \cos \left[\frac{\pi}{2} \beta \left(\frac{1}{2\tau_{n+1}} (\tau_{n+1} + |\omega| - \omega_{n+1}) \right) \right] & \text{if } \omega_{n+1} - \tau_{n+1} \leq |\omega| \leq \omega_{n+1} + \tau_{n+1} \\ \sin \left[\frac{\pi}{2} \beta \left(\frac{1}{2\tau_n} (\tau_n + |\omega| - \omega_n) \right) \right] & \text{if } \omega_n - \tau_n \leq |\omega| \leq \omega_n + \tau_n \\ 0 & \text{otherwise} \end{cases} \quad (4)$$

in which respectively, $\hat{\cdot}$ denotes Fourier transform of a function, ω the circular frequency, β an arbitrary function and τ_n a parameter that determines the
105 size of the transition phase [16] associated with the n -th and $(n + 1)$ -th segments; the transition phase ranges in $[\omega_n - \tau_n, \omega_n + \tau_n]$. One of the most

used forms of β in Eqs. (3) and (4) with a variable x is [22]

$$\beta(x) = \begin{cases} 0 & \text{if } x \leq 0 \\ x^4(35 - 84x + 70x^2 - 20x^3) & \text{if } 0 < x < 1 \\ 1 & \text{if } x \geq 1 \end{cases} \quad (5)$$

The parameter τ_n is calculated by

$$\tau_n = \gamma\omega_n \quad (6)$$

where γ is a sufficiently small parameter, so that it can prevent overlapping
 110 between boundaries of non-zero $\hat{\phi}_1(\omega)$ and $\hat{\psi}_n(\omega)$. A criterion for an acceptable
 value of γ is:

$$\gamma < \min_n \left(\frac{\omega_{n+1} - \omega_n}{\omega_{n+1} + \omega_n} \right) \quad (7)$$

for all n values, and its value can be determined by

$$\gamma = \left(\frac{R-1}{R} \right) \min_n \left(\frac{\omega_{n+1} - \omega_n}{\omega_{n+1} + \omega_n} \right) \quad (8)$$

where R is the number of discrete data in the signal to be decomposed. The
 determination of $\hat{\phi}_1(\omega)$ and $\hat{\psi}_n(\omega)$ concludes the construction of the wavelet
 115 filter bank. Graphical illustrations of $\hat{\phi}_1(\omega)$ and $\hat{\psi}_n(\omega)$ are shown in Figs.
 1(a) and (b), respectively.

After applying a segmentation technique and constructing a filter bank,
 a decomposed signal can be reconstructed as

$$\tilde{f}(t) = W_f^\varepsilon(0, t) * \phi_1(t) + \sum_{n=1}^{N-1} W_f^\varepsilon(n, t) * \psi_n(t) \quad (9)$$

where the asterisk $*$ denotes the convolution of two functions, $W_f^\varepsilon(0, t)$
 120 and $W_f^\varepsilon(n, t)$ are called the approximation coefficient function and detail
 coefficient function, respectively. The function $W_f^\varepsilon(0, t)$ is expressed by

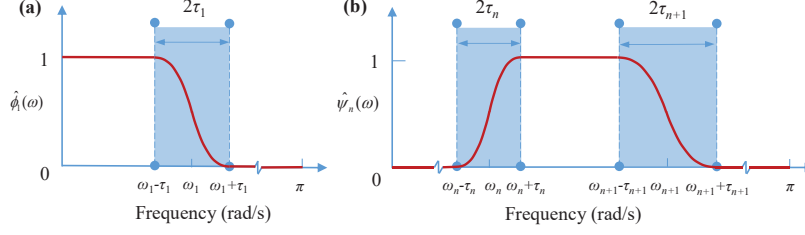


Figure 1: Graphical illustrations of (a) $\hat{\phi}_1(\omega)$ and (b) $\hat{\psi}_n(\omega)$. Shaded parts are transition phases.

$$\begin{aligned}
 W_f^\varepsilon(0, t) &= F^{-1}(\hat{f}(\omega)\hat{\phi}_1(\omega)) \\
 &= \int_{-\omega_1 - \tau_1}^{\omega_1 + \tau_1} f(\tau)\bar{\phi}_1(\tau - t)d\tau
 \end{aligned} \tag{10}$$

where the overbar denotes complex conjugation and F^{-1} denotes the inverse Fourier transform of a function. Note that $F^{-1}(\hat{\phi}_1(\omega)) = \phi_1(t)$ and $F^{-1}(\hat{\psi}_n(\omega)) = \psi_n(t)$. The function $W_f^\varepsilon(n, t)$ is expressed by

$$\begin{aligned}
 W_f^\varepsilon(n, t) &= F^{-1}(\hat{f}(\omega)\hat{\psi}_n(\omega)) \\
 &= \int_{-\omega_{n+1} - \tau_{n+1}}^{\tau_n - \omega_n} f(\tau)\bar{\psi}_n(\tau - t)d\tau + \int_{\omega_n - \tau_n}^{\omega_{n+1} + \tau_{n+1}} f(\tau)\bar{\psi}_n(\tau - t)d\tau
 \end{aligned} \tag{11}$$

125 Resulting decomposed components of the signal can be expressed by

$$f_0(t) = W_f^\varepsilon(0, t) * \phi_1(t) \tag{12}$$

and

$$f_n(t) = W_f^\varepsilon(n, t) * \psi_n(t) \tag{13}$$

A step-by-step description of the EWT for a signal $f(t)$ is provided as follows

Step 1. Obtain a Fourier spectrum of $f(t)$ using Fourier transform.

130 **Step 2.** Segment the spectrum in Step 1 using a segmentation technique, such as the local maxima technique and lowest minimum technique.

Step 3. Construct a wavelet filter bank based on the frequency segments in Step 2.

Step 4. Express approximation and detail coefficient functions based on
135 the wavelet filter bank in Step 3.

Step 5. Decompose $f(t)$ and reconstruct it using in Eq. (9).

The EWT can yield accurate decomposition results when $f(t)$ does not have closely-spaced modes. However, when $f(t)$ has closely-spaced modes, a mode mixing problem can occur due to the transition phase, and the
140 problem can become more serious when the closely-spaced modes exist in high frequencies as τ_n in Eq. (6) becomes larger for higher frequencies.

2.2. FDM

Assume that $f(u)$ is zero-mean, discrete, and a length-limited signal within one period U , which is an even integer; the fundamental frequency of
145 $f(u)$ can be expressed by

$$\varphi_0 = \frac{2\pi}{U} \quad (14)$$

In the FDM, $f(u)$ is approximated by a summation of K orthogonal FIBFs $g_k(u)$ [20]:

$$f(u) = \sum_{k=1}^K g_k(u) \quad (15)$$

Based on Eq. (15), the analytical signal of $f(u)$ can be expressed by [24]

$$\begin{aligned}
z(u) &= f(u) + jH(f(u)) \\
&= \sum_{k=1}^K [g_k(u) + jH(g_k(u))] \\
&= \sum_{k=1}^K z_k(u)
\end{aligned} \tag{16}$$

where $H(\cdot)$ denotes Hilbert transform of a function, $j = \sqrt{-1}$, and $z_k(u) =$
150 $g_k(u) + jH(g_k(u))$. The term $z_k(u)$ can be considered as the analytical signal
corresponding to $g_k(u)$. Note that $z(u)$ can be expressed as Fourier series:

$$z(u) = \sum_{m=1}^{U/2-1} a_m e^{jm\varphi_0 u} \tag{17}$$

where

$$a_m = \frac{2}{U} \sum_{u=0}^{U-1} f(u) e^{-jm\varphi_0 u} \tag{18}$$

and values of a_m can be estimated using discrete Fourier transform.

The analytical signal $z_k(u)$ can be considered as a filtered signal by
155 Hilbert transform filter [25], which is the counterpart of a filter in the wavelet
filter bank in the EWT, and $z_k(u)$ can be further expressed by

$$z_k(u) = \sum_{m=M_{k-1}+1}^{M_k} a_m e^{jm\varphi_0 u} \tag{19}$$

where M_k ranges from 1 to $(U/2 - 1)$ with $M_0 = 0$. Determination of values
of M_k is similar to the segmentation in the EWT. In the FDM, two frequency
scan techniques have been proposed to determine the values of M_k in Eq.
160 (19), including the LTH technique and the HTL technique [20]. Flowcharts

of the LTH and HTL techniques are shown in Figs. 2 and 3, respectively. In the LTH technique, K values of M_k are searched in a forward manner so that $M_1 < M_2 < \dots < M_k \dots < M_K$, with which

$$\begin{aligned}
z_1(u) &= \sum_{m=M_0+1}^{M_1} a_m e^{jm\varphi_0 u} \\
z_2(u) &= \sum_{m=M_1+1}^{M_2} a_m e^{jm\varphi_0 u} \\
&\vdots \\
z_K(u) &= \sum_{m=M_{K-1}+1}^{M_K} a_m e^{jm\varphi_0 u}
\end{aligned} \tag{20}$$

where $M_0 = 0$ and $M_K = U/2 - 1$. The signal $z_k(u)$ can further be expressed
165 by

$$z_k(u) = A_k(u) e^{j\theta_k(u)} \tag{21}$$

where

$$A_k(u) = \left\| \sum_{m=M_{k-1}+1}^{M_k} a_m e^{jm\varphi_0 u} \right\|_2 \tag{22}$$

and

$$\theta_k(u) = \arg \left[\sum_{m=M_{k-1}+1}^{M_k} a_m e^{jm\varphi_0 u} \right] \tag{23}$$

denote instantaneous amplitude and phase of $z_k(u)$, respectively, in which $\|\cdot\|_2$ and $\arg(\cdot)$ calculate Euclidean norm and argument of a complex quantity,

170 respectively. The FIBFs $g_k(u)$ can be obtained by

$$g_k(u) = \text{Re} \left[A_k(u) e^{j\theta_k(u)} \right] \quad (24)$$

where $\text{Re}(\cdot)$ is the real part of a function. In the HTL technique, K values of M_k are searched in a backward manner so that $M_K < \dots < M_k < M_{k-1} < \dots < M_1$, with which

$$\begin{aligned} z_1(u) &= \sum_{m=M_1}^{M_0-1} a_m e^{jm\varphi_0 u} \\ z_2(u) &= \sum_{m=M_2}^{M_1-1} a_m e^{jm\varphi_0 u} \\ &\vdots \\ z_K(u) &= \sum_{m=M_K}^{M_{K-1}-1} a_m e^{jm\varphi_0 u} \end{aligned} \quad (25)$$

where $M_0 = U/2$ and $M_K = 1$.

175 A step-by-step description of the FDM for $f(u)$ is as follows

Step 1. Obtain a Fourier spectrum of $f(u)$ using Fourier transform.

Step 2. Express $z(u)$ using the spectrum of $f(u)$ obtained in Step 1.

Step 3. Obtain K $z_k(u)$ using the LTH or HTL technique.

Step 4. Obtain FIBFs $g_k(u)$ from the real part of $z_k(u)$ obtained in Step

180 3.

Step 5. Reconstruct $f(u)$ as a summation of FIBFs $g_k(u)$ obtained in Step 4.

An issue of the FDM is that its decomposition results using the LTH technique can be inconsistent with that using the HTL technique, and the

185 issue will be verified in the numerical investigation in Sec. 4.

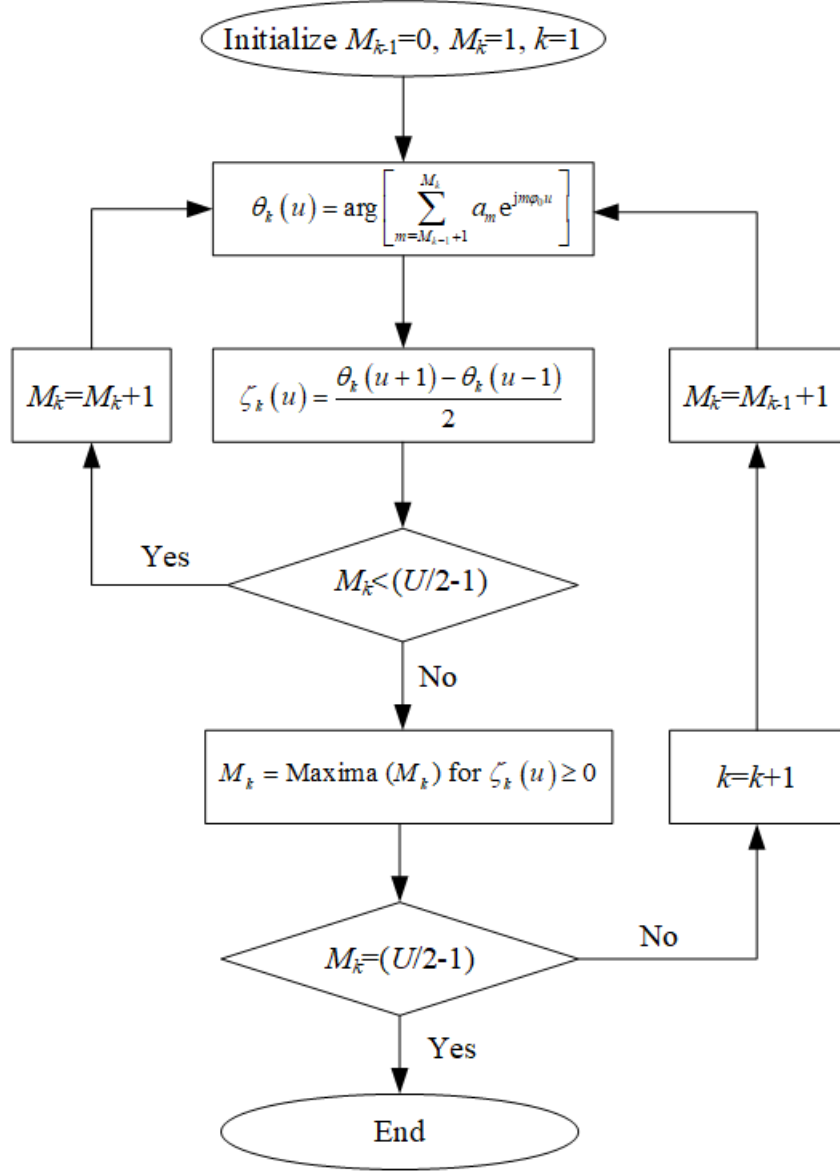


Figure 2: Flowchart of the LTH technique.

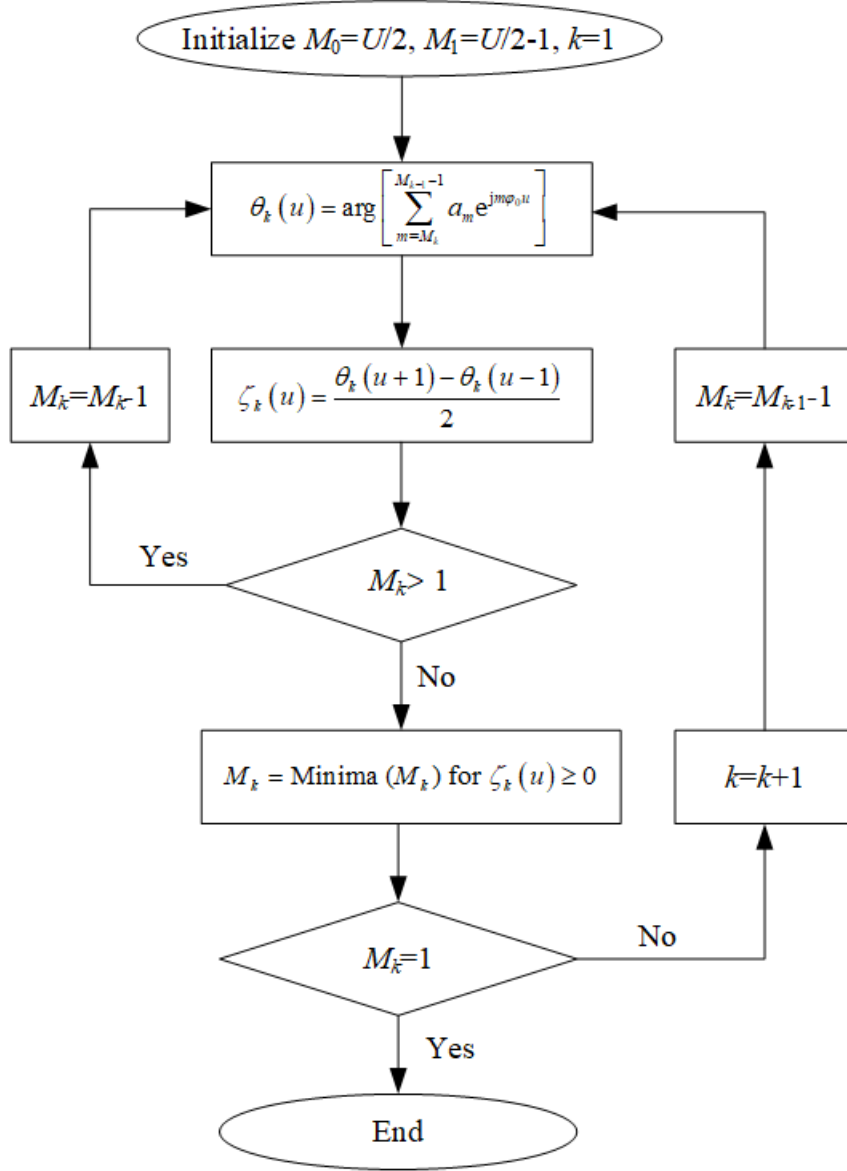


Figure 3: Flowchart of the HTL technique.

3. EFD

Similar to the EWT and FDM, the EFD consists of two critical steps: an improved segmentation technique and construction of an ideal filter bank. In the EFD, Fourier spectrum of a signal to be decomposed is defined on a normalized frequency range $[-\pi, \pi]$, and the improved segmentation technique and construction of an ideal filter bank for the spectrum in the frequency range $[0, \pi]$ are described below.

3.1. Improved segmentation technique

The improved segmentation technique is proposed based on the lowest minima technique [23] described in Sec. 2.1. In the improved segmentation technique, $[0, \pi]$ is divided into N contiguous frequency segments. Unlike the local maxima and lowest minima techniques, ω_0 and ω_N are not necessarily equal to 0 and π , respectively, and their values are determined in an adaptive sorting process. In the sorting process, Fourier spectrum magnitudes at $\omega = 0$ and $\omega = \pi$ and their local maxima are identified and extracted to a series. All magnitudes in the series are sorted in descending order. Frequencies corresponding to the first N largest values in the sorted series are denoted by $[\Omega_1, \Omega_2, \dots, \Omega_N]$. In addition, $\Omega_0 = 0$ and $\Omega_{N+1} = \pi$ are defined. Boundaries of each segment are determined by

$$\omega_n = \begin{cases} \arg \min_{\omega} \check{X}_n(\omega) & \text{if } 0 \leq n \leq N \text{ and } \Omega_n \neq \Omega_{n+1} \\ \Omega_n & \text{if } 0 \leq n \leq N \text{ and } \Omega_n = \Omega_{n+1} \end{cases} \quad (26)$$

where $\check{X}_n(\omega)$ denotes the Fourier spectrum magnitudes between Ω_n and Ω_{n+1} , which concludes the improved segmentation technique.

3.2. Construction of an ideal filter bank

Both the EWT and FDM consist of a step of constructing a filter bank. In the EWT, a wavelet filter bank is formed by the empirical scaling function and wavelet functions. In the FDM, Hilbert transform filter bank is constructed based on Fourier spectrum of the analytical signal associated with a signal to be decomposed. In the EFD, an ideal filter bank is constructed based on frequency segments obtained by the improved segmentation technique. In each frequency segment, the ideal filter is a band-pass filter with ω_{n-1} and ω_n serving as its cut-off frequencies and it has not transition phases. Hence, the ideal filter can retain the major Fourier spectrum component in the segment and all other Fourier spectrum components beyond the segment are excluded.

Fourier transform of a signal to be decomposed $f(t)$ is expressed as

$$\hat{f}(\omega) = \int_{-\infty}^{\infty} f(t)e^{-j\omega t} dt \quad (27)$$

An ideal filter bank can be constructed by $\hat{\mu}_n(\omega)$:

$$\hat{\mu}_n(\omega) = \begin{cases} 1 & \text{if } \omega_{n-1} \leq |\omega| \leq \omega_n \\ 0 & \text{otherwise} \end{cases} \quad (28)$$

where $1 \leq n \leq N$ and values of ω_n are determined by Eq. (26). A graphical illustration of the ideal filter bank is shown in Fig. 4.

Filtered signals that correspond to $\hat{\mu}_n(\omega)$ are calculated by

$$\hat{f}_n(\omega) = \hat{\mu}_n(\omega)\hat{f}(\omega) = \begin{cases} \hat{f}(\omega) & \text{if } \omega_{n-1} \leq |\omega| \leq \omega_n \\ 0 & \text{otherwise} \end{cases} \quad (29)$$

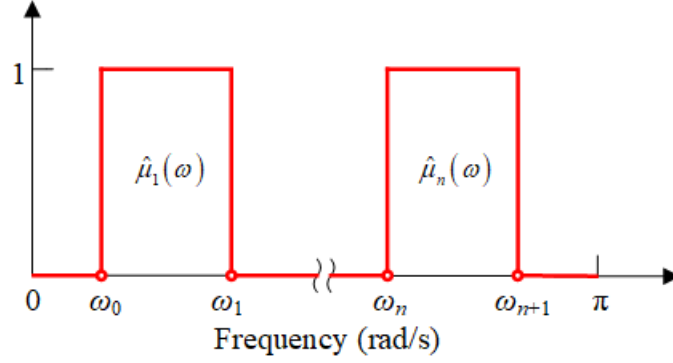


Figure 4: Graphical illustration of an ideal filter bank of the EFD.

Decomposed components in the time domain can be obtained using the
 225 inverse Fourier transform:

$$\begin{aligned}
 f_n(t) &= F^{-1} [\hat{f}_n(\omega)] = \int_{-\infty}^{\infty} \hat{f}_n(\omega) e^{j\omega t} d\omega \\
 &= \int_{-\omega_n}^{-\omega_{n-1}} \hat{f}(\omega) e^{j\omega t} d\omega + \int_{\omega_{n-1}}^{\omega_n} \hat{f}(\omega) e^{j\omega t} d\omega \quad (30)
 \end{aligned}$$

The reconstructed signal is calculated as a summation of all decomposed components:

$$\tilde{f}(t) = \sum_{n=1}^N f_n(t) \quad (31)$$

A flowchart of the EFD is shown in Fig. 5 and a step-by-step description of the EFD is provided as follows.

230 **Step 1.** Obtain Fourier spectrum of a signal to be decomposed $f(t)$ using Fourier transform.

Step 2. Determine boundaries of segment ω_n using the improved segmentation technique based on Fourier spectrum obtained in Step 1.

Table 1: Numbers of modes to be decomposed for.

Signal	Decomposition method		
	EFD	EWT	VMD
$f_{\text{Sig1}}(t)$	3	3	-
$f_{\text{Sig2}}(t)$	3	4	-
$f_{\text{Sig3}}(t)$	2	2	2
$f_{\text{Sig4}}(t)$	3	3	3
$f_{\text{Sig5}}(t)$	3	4	3
$f_{\text{Sig6}}(t)$	2	3	2

Step 3. Construct an ideal filter bank $\hat{\mu}_n(\omega)$ based on ω_n obtained in
 235 Step 2.

Step 4. Obtain filtered signals $\hat{f}_n(\omega)$ in the frequency domain using
 $\hat{\mu}_n(\omega)$ obtained in Step 3.

Step 5. Obtain decomposed components $f_n(t)$ in the time-domain using
 inverse Fourier transforms of $\hat{f}_n(\omega)$ obtained in Step 4

240 4. Numerical investigation

In this section, the effectiveness of the lowest minima and improved
 segmentation techniques are compared based on two typical signals that have
 multiple modes, denoted by $f_{\text{Sig1}}(t)$ and $f_{\text{Sig2}}(t)$. Decomposition accuracy of
 the proposed EFD method is compared with those of the EWT [16], FDM
 245 [20], VMD [13] and EMD [7] methods for two typical non-stationary time-
 domain signals $f_{\text{Sig3}}(t)$ and $f_{\text{Sig4}}(t)$, and two stationary time-domain signals
 $f_{\text{Sig5}}(t)$ and $f_{\text{Sig6}}(t)$, with closely-spaced modes. For the EFD, EWT and
 VMD, the numbers of decomposed modes are listed in Table 1.

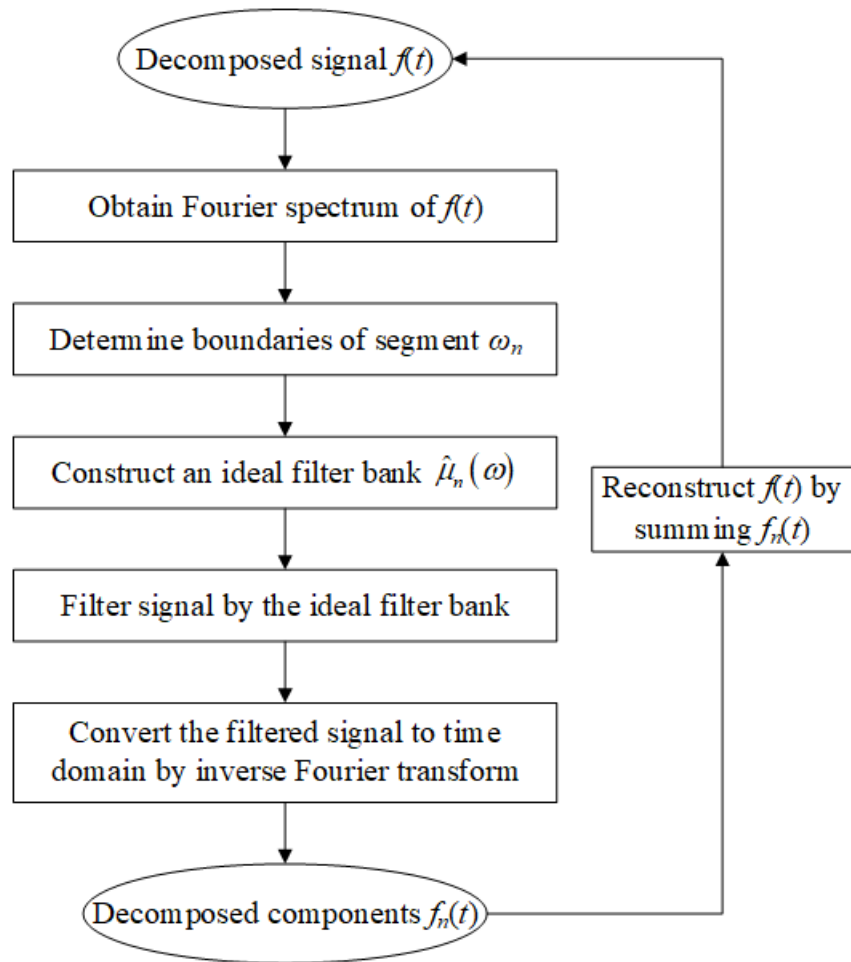


Figure 5: Flowchart of the EFD.

4.1. Comparison of segmentation techniques

250 The signals $f_{\text{Sig1}}(t)$ and $f_{\text{Sig2}}(t)$ are expressed by

$$f_{\text{Sig1}}(t) = 6t + \cos(24\pi t) + \cos(50\pi t) + \delta(t) \quad (32)$$

and

$$f_{\text{Sig2}}(t) = \cos(20\pi t) + \cos(24\pi t) + \cos(50\pi t) + \delta(t) \quad (33)$$

where $\delta(t)$ is a random white-noise such that $f_{\text{Sig1}}(t)$ and $f_{\text{Sig2}}(t)$ have signal-to-noise-ratios of 10 dB. Segmentation results of $f_{\text{Sig1}}(t)$ by the lowest minima and improved segmentation techniques are shown in Fig. 6: the first two
255 segments by the two techniques are the same, but the last segment in the improved segmentation technique has a narrower frequency range than that by the lowest minima technique. Therefore, the improved segmentation technique can alleviate the effect of noise on the decomposed component associated with the last segment. Segmentation results of $f_{\text{Sig2}}(t)$ by the
260 lowest minima and improved segmentation techniques are shown in Fig. 7. The first segment by the lowest minima technique, shown in Fig. 7(a), can be considered trivial as it does not contain a meaningful Fourier spectrum component and its associated decomposed component consists of noise only. On the other hand, the trivial segment is excluded in segmentation results
265 by the improved segmentation technique, shown in Fig. 7(b), and its first resulting segment contains a meaningful Fourier spectrum component. Segmentation results of the last segments by the two techniques are similar to those of $f_{\text{Sig1}}(t)$: the decomposed component associated with the improved segmentation technique has a lower level of noise than that by the lowest minima technique.

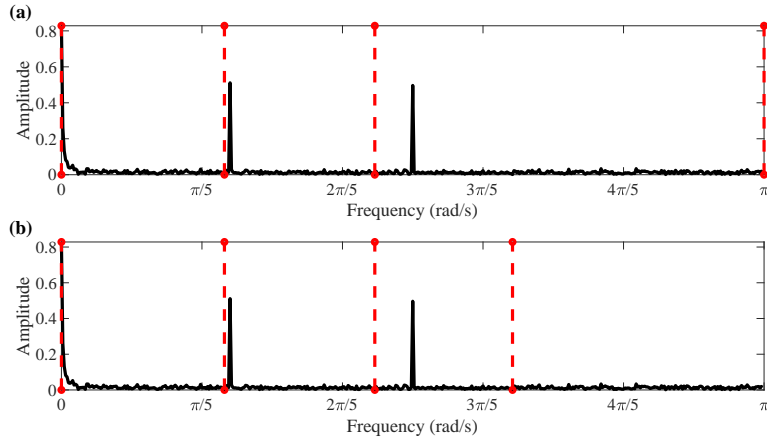


Figure 6: Segmentation results of $f_{\text{Sig1}}(t)$ by (a) the lowest minima technique and (b) the improved segmentation technique.

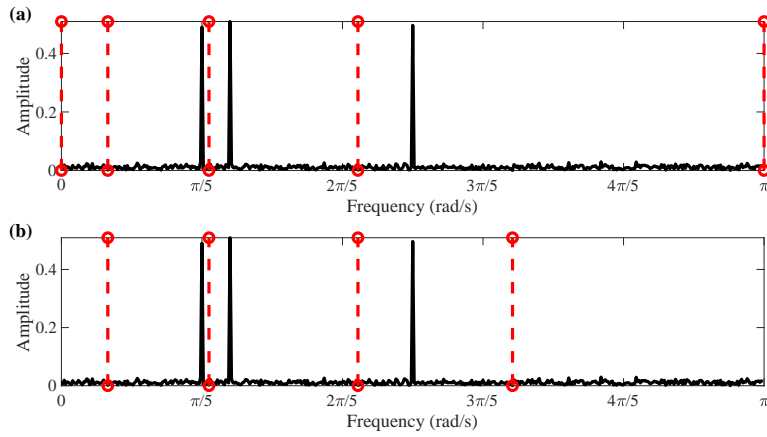


Figure 7: Segmentation results of $f_{\text{Sig2}}(t)$ by (a) the lowest minima technique and (b) the improved segmentation technique.

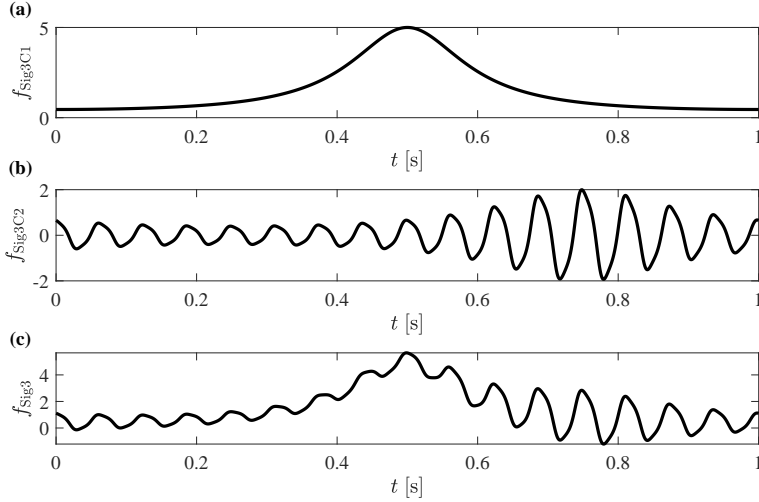


Figure 8: (a) Modes f_{Sig3C1} , (b) f_{Sig3C2} and (c) the non-stationary signal $f_{\text{Sig3}}(t)$ that consists of the two modes in (a) and (b) as expressed in Eq. (34).

270 *4.2. Non-stationary multimode signals*

The non-stationary multimode signal $f_{\text{Sig3}}(t)$ is expressed by

$$\begin{cases} f_{\text{Sig3C1}}(t) &= \frac{1}{1.2 + \cos(2\pi t)} \\ f_{\text{Sig3C2}}(t) &= \frac{\cos(32\pi t + 0.2 \cos(64\pi t))}{1.5 + \sin(2\pi t)} \\ f_{\text{Sig3}}(t) &= f_{\text{Sig3C1}}(t) + f_{\text{Sig3C2}}(t) \end{cases} \quad (34)$$

The signal $f_{\text{Sig3}}(t)$ consists of two modes f_{Sig3C1} and f_{Sig3C2} in Eq. (34), which are shown in Figs. 8(a) and (b) [26], and $f_{\text{Sig3}}(t)$ is similar to the expression of a solution to Duffing equation [7]. The signal $f_{\text{Sig3}}(t)$ is sampled at a
 275 frequency of 1000 Hz for one second and shown in Fig. 8(c).

Decomposition results of $f_{\text{Sig3}}(t)$ by the EFD, EWT, FDM-LTH, FDM-HTL, VMD, and EMD are shown in Fig. 9. Root-mean-square errors (RMSEs) between the decomposition results and analytical ones are calculated

Table 2: Results of the RMSEs for $f_{\text{Sig3}}(t)$.

Component	Decomposition method					
	EFD	EWT	FDM-LTH	FDM-HTL	VMD	EMD
f_{Sig3C1}	1.12×10^{-2}	4.19×10^{-2}	2.43×10^{-2}	2.11×10^{-1}	3.74×10^{-2}	9.54×10^{-3}
f_{Sig3C2}	9.85×10^{-3}	2.12×10^{-2}	7.89×10^{-2}	2.24×10^{-1}	5.41×10^{-2}	9.54×10^{-3}

by

$$\text{RMSE} = \sqrt{\frac{1}{R} \sum_{r=1}^R |y_r - \tilde{y}_r|^2} \quad (35)$$

280 where y_r is the analytical component at the r -th discrete instant, and \tilde{y}_r is the corresponding component at the r -th discrete instant obtained by a decomposition method. RMSEs associated with the aforementioned decomposition methods are calculated and listed in Table 2. For f_{Sig3C1} , it can be seen that the RMSE associated with the EMD is the smallest and that associated with the EFD is the second smallest. While the RMSEs associated with the EWT, VMD and FDM-LTH are relatively small, that associated with the FDM-HTL is large. For f_{Sig3C2} , results similar to f_{Sig3C1} can be observed: RMSEs associated with the EMD and EFD are the smallest, and the RMSEs of the EWT, VMD and FDM-LTH are relatively small. In addition, the RMSE associated with the FDM-HTL is also large. It is indicated that the EFD can accurately decompose the non-stationary multimode signal. The inconsistency of decomposition results by the FDM-LTH and FDM-HTL is verified.

290

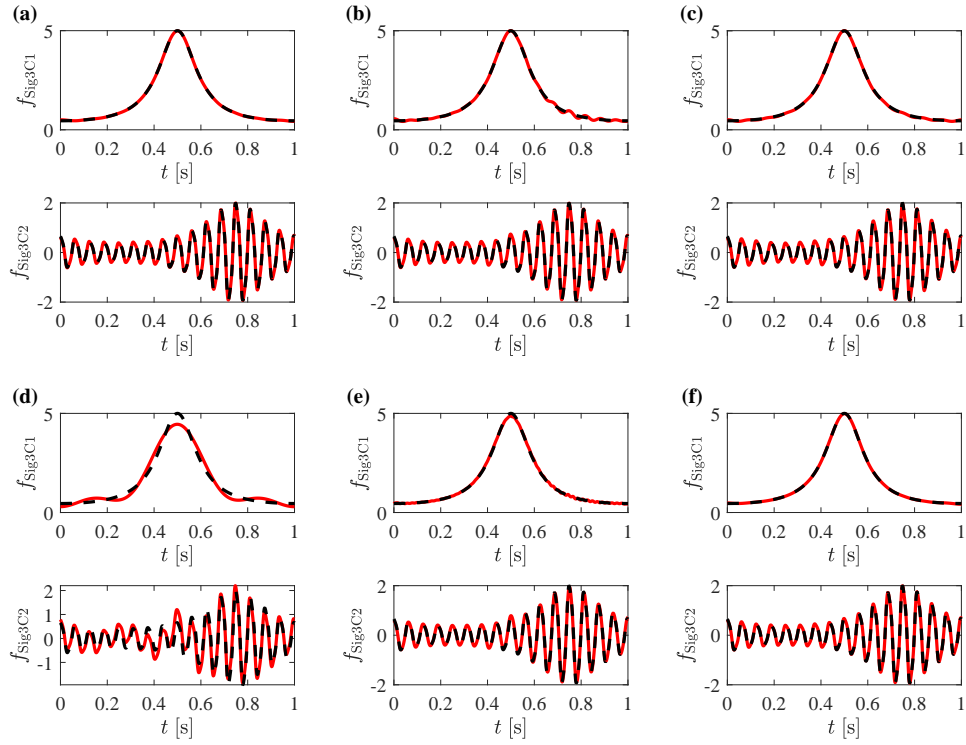


Figure 9: Comparisons between the analytical components of $f_{\text{Sig}3}(t)$ (dashed lines) in Eq. (34) and decomposition results of $f_{\text{Sig}3}(t)$ (solid line) by the (a) EFD, (b) EWT, (c) FDM-LTH, (d) FDM-HTL, (e) VMD, and (f) EMD.

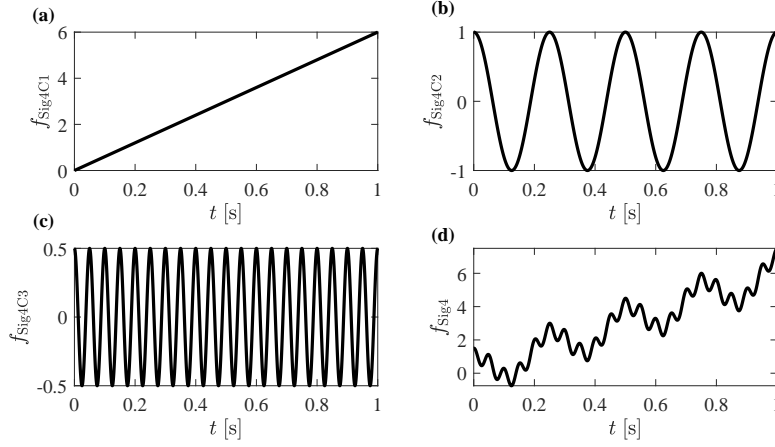


Figure 10: (a) Modes f_{Sig4C1} , (b) f_{Sig4C2} , (c) f_{Sig4C3} and (d) the non-stationary signal $f_{\text{Sig4}}(t)$ that consists of the three modes in (a), (b) and (c) as expressed in Eq. (36).

Another non-stationary multimode signal $f_{\text{Sig4}}(t)$ is expressed by [26]

$$\begin{cases} f_{\text{Sig4C1}}(t) &= 6t \\ f_{\text{Sig4C2}}(t) &= \cos(8\pi t) \\ f_{\text{Sig4C3}}(t) &= 0.5 \cos(40\pi t) \\ f_{\text{Sig4}}(t) &= f_{\text{Sig4C1}}(t) + f_{\text{Sig4C2}}(t) + f_{\text{Sig4C3}}(t) \end{cases} \quad (36)$$

295 The signal $f_{\text{Sig4}}(t)$ consists of three modes: one mode f_{Sig4C1} with a monotonically increasing amplitude as shown in Fig. 10(a) and two modes f_{Sig4C2} and f_{Sig4C3} with sinusoidal amplitudes as shown in Figs. 10(b) and (c), respectively. The signal $f_{\text{Sig4}}(t)$ is sampled at a frequency of 1000 Hz for one second and shown in Fig. 10(d).

300 The EFD, EWT, FDM-LTH, FDM-HTL, VMD and EMD are employed to decompose the sampled $f_{\text{Sig4}}(t)$. Their results are compared with the analytical ones as shown in Fig. 11 and corresponding RMSEs in Eq. (35) are calculated and listed in Table 3. For f_{Sig4C1} , the RMSE associated with

Table 3: Results of the RMSEs for $f_{\text{Sig4}}(t)$.

Component	Decomposition method					
	EFD	EWT	FDM-LTH	FDM-HTL	VMD	EMD
f_{Sig4C1}	4.67×10^{-2}	1.07×10^{-1}	1.08×10^0	1.08×10^0	8.40×10^{-2}	6.46×10^{-2}
f_{Sig4C2}	8.33×10^{-2}	2.23×10^{-1}	1.02×10^0	1.02×10^0	9.14×10^{-2}	6.38×10^{-2}
f_{Sig4C3}	7.01×10^{-3}	7.43×10^{-2}	3.81×10^{-1}	3.98×10^{-1}	9.93×10^{-3}	8.10×10^{-3}

the EFD is the smallest, and those associated with the EWT, VMD and EMD
305 are relatively small. RMSEs associated with the FDM-LTH and FDM-HTL
are large. For f_{Sig4C2} , RMSE associated the EMD is the smallest and those
associated with the EFD and VMD are slightly larger than that associated
with the EMD. The RMSEs associated with the EWT, FDM-LTH and FDM-
HTL are large and that associated with the FDM is the largest. For f_{Sig4C3} ,
310 the RMSE associated with the EFD is the smallest while those associated
with the VMD and EMD are slightly larger than that associated with the
EFD. Similar to the observations for f_{Sig4C2} , the RMSEs associated with
the EWT, FDM-TLH and FDM-HTL are larger than others. It is indicated
again that the EFD can accurately decompose a nonstationary multimode
315 signal. In addition, it is shown that both the FDM-LTH and FDM-HTL can
yield inaccurate decomposition results.

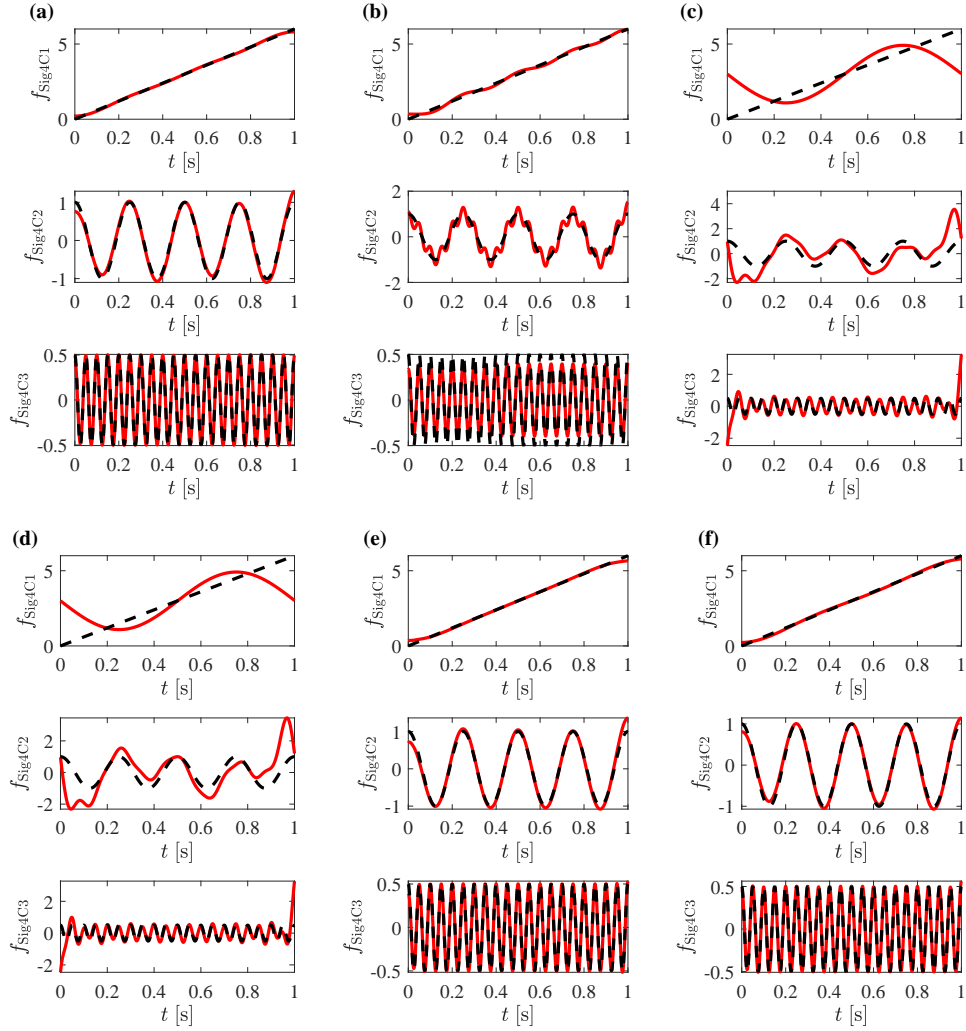


Figure 11: Comparisons between the analytical components of $f_{\text{Sig4}}(t)$ (dashed lines) in Eq. (36) and decomposition results of $f_{\text{Sig4}}(t)$ (solid line) by the (a) EFD, (b) EWT, (c) FDM-LTH, (d) FDM-HTL, (e) VMD, and (f) EMD.

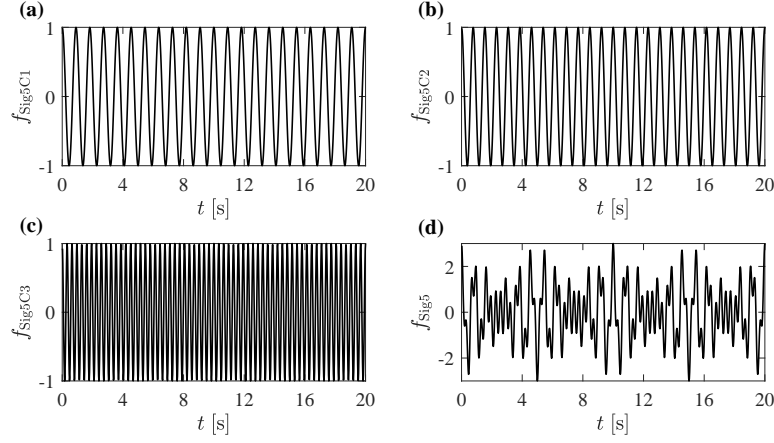


Figure 12: (a) Modes f_{Sig5C1} , (b) f_{Sig5C2} , (c) f_{Sig5C3} and (d) $f_{\text{Sig5}}(t)$ that consists of the three modes in (a), (b) and (c) which are expressed in Eq. (37).

4.3. Closely-spaced modes

A stationary signal $f_{\text{Sig5}}(t)$ with two closely-spaced modes is expressed by

$$\begin{cases} f_{\text{Sig5C1}}(t) = \cos(2\pi\lambda_a t) \\ f_{\text{Sig5C2}}(t) = \cos(2\pi\lambda_b t) \\ f_{\text{Sig5C3}}(t) = \cos(2\pi\lambda_c t) \\ f_{\text{Sig5}}(t) = f_{\text{Sig5C1}}(t) + f_{\text{Sig5C2}}(t) + f_{\text{Sig5C3}}(t) \end{cases} \quad (37)$$

320 where $\lambda_a=1.1$ Hz, $\lambda_b=1.3$ Hz and $\lambda_c=3.1$ Hz, and it consists of a pair of closely-spaced modes shown in Figs. 12(a) and (b) and, a mode with a frequency greatly larger than those of the closely-spaced modes is shown in Fig. 12(c). The signal $f_{\text{Sig5}}(t)$ is sampled at a frequency of 50 Hz for 20 seconds and shown in Fig. 12(d).

325 The EFD, EWT, FDM-LTH, FDM-HTL, VMD, and EMD are used to decompose the sampled $f_{\text{Sig5}}(t)$. Their results are shown in Fig. 13 and

Table 4: Results of the RMSEs for $f_{\text{Sig5}}(t)$.

Component	Decomposition method					
	EFD	EWT	FDM-LTH	FDM-HTL	VMD	EMD
f_{Sig4C1}	2.20×10^{-2}	1.11×10^{-1}	7.07×10^{-1}	0.00	1.90×10^{-2}	7.02×10^{-1}
f_{Sig4C2}	1.60×10^{-2}	1.10×10^{-1}	7.07×10^{-1}	0.00	1.50×10^{-2}	6.94×10^{-1}
f_{Sig4C3}	1.20×10^{-2}	1.20×10^{-2}	0.00	0.00	1.41×10^{-2}	4.58×10^{-2}

corresponding RMSEs in Eq. (36) are calculated and listed in Table 4. Note that in the decomposition result by the FDM-LTH, only two components are obtained as f_{Sig5C1} and f_{Sig5C2} exist in the first component and RMSEs corresponding to f_{Sig5C1} and f_{Sig5C2} are mixed as one mode. For f_{Sig5C1} , the RMSE associated with the FDM-HTL is the smallest and those associated with the VMD and EFD are relatively small, and those associated with the EWT, FDM-LTH and EMD are large. For f_{Sig5C2} , similar observations can be obtained: the RMSE associated with the FDM-HTL is the smallest, those associated with the VMD and EFD are relatively small, and those associated with EWT, FDM-LTH and EMD are large. For f_{Sig5C3} , the RMSEs associated with the FDM-LTH and FDM-HTL are the smallest and those associated with other methods are relatively small. It is indicated that the EFD can yield decomposition results for signals with closely-spaced modes with higher accuracy than the EWT and EMD. In addition, the inconsistency between decomposition results by the FDM-LTH and FDM-HTL is verified again.

Another stationary signal with two modes [27] denoted by $f_{\text{Sig6}}(t)$ is constructed to further compare performances of the different decomposition

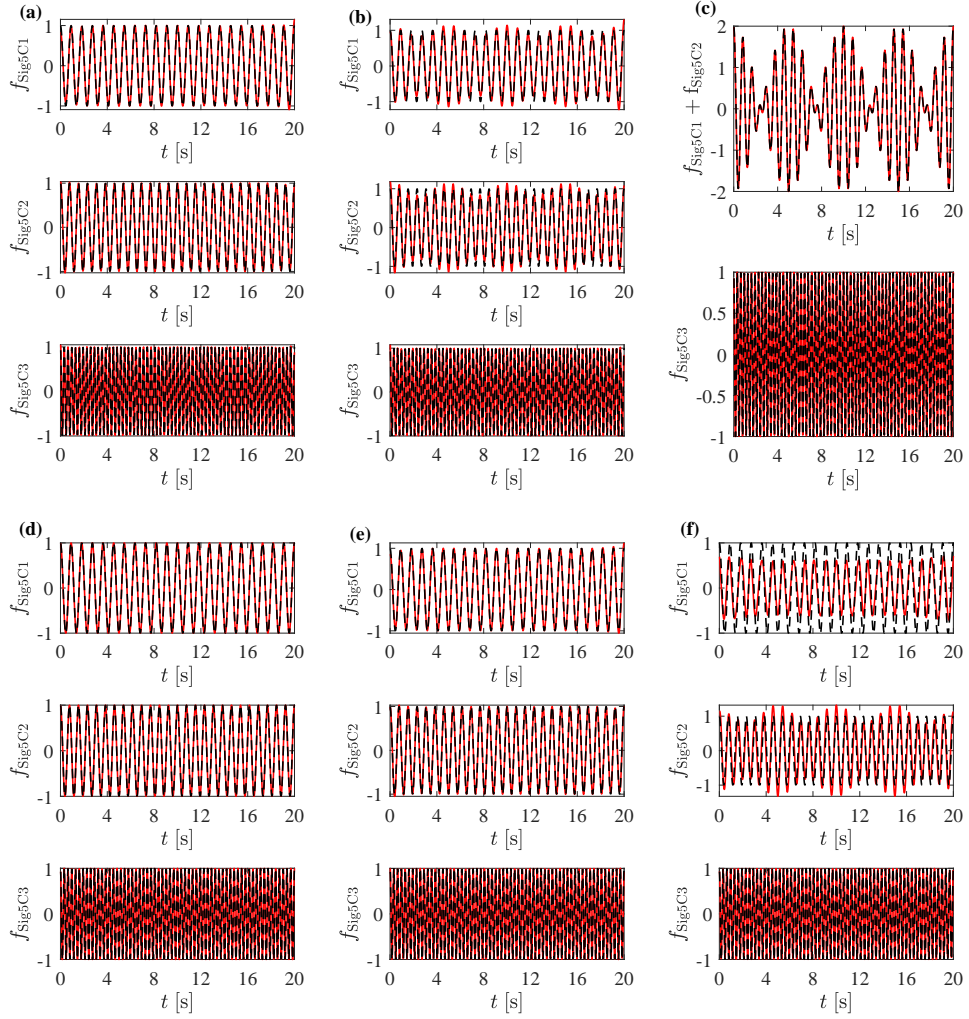


Figure 13: Comparisons between the analytical components of $f_{\text{Sig}5}(t)$ (dashed lines) in Eq. (37) and decomposition results of $f_{\text{Sig}5}(t)$ (solid line) by the (a) EFD, (b) EWT, (c) FDM-LTH, (d) FDM-HTL, (e) VMD, and (f) EMD.

345 methods for signals with closely-spaced modes, which is expressed by

$$\begin{cases} f_{\text{Sig6C1}}(t) &= \cos(2\pi t) \\ f_{\text{Sig6C2}}(t) &= a \cos(2\pi \lambda_r t) \\ f_{\text{Sig6}}(t) &= f_{\text{Sig6C1}}(t) + f_{\text{Sig6C2}}(t) \end{cases} \quad (38)$$

where a and λ_r denote a ratio between the amplitudes of $f_{\text{Sig6C2}}(t)$ and $f_{\text{Sig6C1}}(t)$ and that between the frequencies of $f_{\text{Sig6C2}}(t)$ and $f_{\text{Sig6C1}}(t)$, respectively; $0.01 \leq a \leq 100$ and $0.01 \leq \lambda_r \leq 1$. When λ_r approaches to 1, $f_{\text{Sig6C2}}(t)$ and $f_{\text{Sig6C1}}(t)$ become closely-spaced modes. The signal $f_{\text{Sig6}}(t)$ is sampled
 350 at a frequency of 10 Hz for 300 seconds. The EFD, EWT, FDM-LTH, FDM-HLT, VMD and EMD are deployed to decompose $f_{\text{Sig6}}(t)$. A two-dimensional binary quantity $Q(a, \lambda_r)$ is used to measure the decomposition performance [27] of the different methods for $f_{\text{Sig6}}(t)$ with different values of a and λ_r , and it is expressed by

$$Q(a, \lambda_r) = \begin{cases} 0 & \text{if } \frac{\|C1 - f_{\text{Sig6C1}}\|_2}{\|f_{\text{Sig6C2}}\|_2} \leq \varepsilon \\ 1 & \text{if } \frac{\|C1 - f_{\text{Sig6C1}}\|_2}{\|f_{\text{Sig6C2}}\|_2} > \varepsilon \end{cases} \quad (39)$$

355 where C1 is the decomposed component by a decomposition method corresponding to $f_{\text{Sig6C1}}(t)$ and ε is the threshold of Q . A zero value and a unit value of Q indicate an acceptable decomposition result and an unacceptable decomposition one, respectively, and the value of ε is chosen to be 0.5 in this study, which was also the cases in Refs. [4, 12, 27]. Resulting $Q(a, \lambda_r)$ corresponding
 360 to the six methods are shown in Fig. 14, where the colors of blue and yellow correspond to Q values of 0 and 1, respectively. It can be seen that the yellow area corresponding to the EFD is the smallest among the six Q results. Even as λ_r approaches to 1, $f_{\text{Sig6}}(t)$ can still be well decomposed.

However, the decomposition by the EFD is affected when a approaches to
 365 0.01. Further, the yellow area corresponding to the EWT is the second
 smallest but its decomposition performance is affected when a approaches to
 0.01 and λ_r is larger than 0.8. The yellow area corresponding to the VMD is
 the third smallest. Similar to Q corresponding to the EFD, as λ_r approaches
 to 1, $f_{\text{Sig6}}(t)$ can still be well decomposed. However, the decomposition
 370 performance associated with the VMD is affected when a is close to 0.01
 and 100. The yellow area corresponding to the EMD is the fourth smallest.
 The EMD cannot decompose $f_{\text{Sig6}}(t)$, when λ_r is larger than 0.65 for all a .
 In addition, worse decomposition results are obtained when a approaches to
 100. For the FDM-LTH and FDM-HTL, decomposition performances are
 375 almost the same but the worst among the six methods. Their decomposition
 results are greatly affected by the value of a . They can hardly decompose
 $f_{\text{Sig6}}(t)$, when a is smaller than 1 for $\lambda_r \geq 0.01$. Based on the observations, it
 is indicated that the EFD can robustly and accurately decompose $f_{\text{Sig6}}(t)$ as
 its decomposition results are the most accurate even when $f_{\text{Sig6}}(t)$ becomes
 380 a signal with closely-spaced modes, and both the FDM-LTH and FDM-HTL
 can yield inaccurate decomposition results for $f_{\text{Sig6}}(t)$.

4.4. TFR

TFRs of $f_{\text{Sig3}}(t)$ of components decomposed by the six methods are
 compared to further study their performances. TFR of decomposed components
 385 by the EFD, EWT, VMD and EMD are calculated using Hilbert transform
 and those by the FDM-HTL and FDM-LTH are directly obtained as instantaneous
 amplitude and frequency. A benchmark TFR is obtained by using Hilbert
 transforms of theoretical components. TFRs corresponding to six decomposition
 methods and the benchmark one are shown in Fig. 15 and RMSEs corresponding

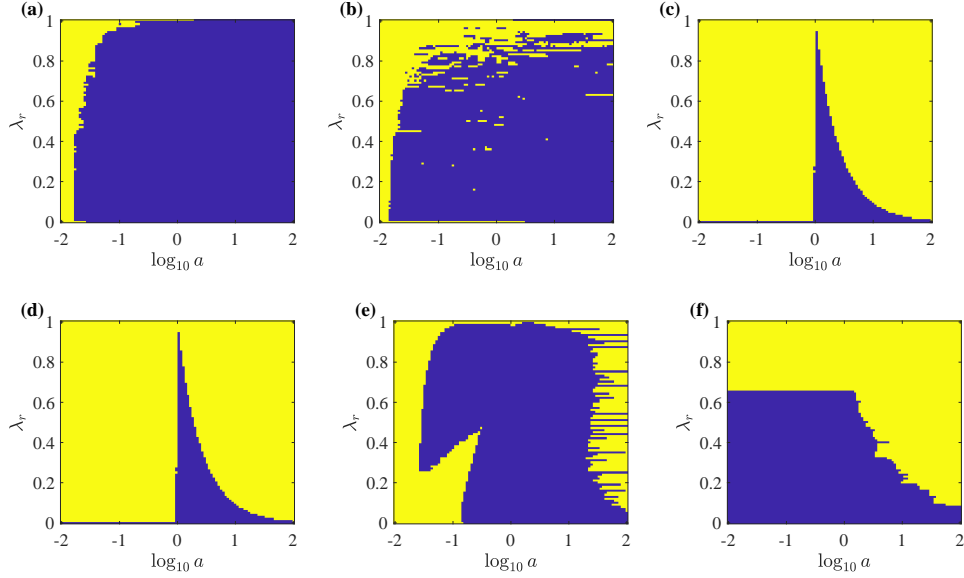


Figure 14: Decomposition performance with respect to (a, λ_r) by the (a) EFD, (b) EWT, (c) FDM-LTH, (d) FDM-HTL, (e) VMD and (f) EMD.

390 to TFR are calculated and listed in Table 5. From Fig. 15, it can be found that the TFRs associated with the EFD and FDM-LTH compare well with the benchmark one, while the comparisons between the TFRs associated with the EWT and EMD and the benchmark one are acceptable. However, large differences can be observed for the TFRs corresponding to the VMD
395 and FDM-HTL with the benchmark one.

In addition, RMSEs of between magnitudes in the TFRs by the six methods and those in the benchmark TFR at all frequencies and times are calculated and listed in Table 5. It can be seen that the RMSEs associated with the TFRs by the EFD and EWT are the smallest. Those associated
400 with the TFR by the EMD are relatively small, while those associated with the TFRs by the FDM-LTH, FDM-HTL and VMD are large. The TFRs

Table 5: Calculated RMSEs of TFR associated with $f_{\text{Sig3}}(t)$.

EFD	EWT	FDM-LTH	FDM-HTL	VMD	EMD
1.24×10^{-1}	1.24×10^{-1}	1.35×10^{-1}	1.38×10^{-1}	1.36×10^{-1}	1.29×10^{-1}

shown in Fig. 15 and the RMSEs in Table 5 show that the EFD can yield accurate TFR, and the inconsistency between TFR results by the FDM-LTH and FDM-HTL is observed.

405 4.5. Computational cost

To explore the computational cost of the EFD, computation times by the EFD, EWT, FDM, VMD and EMD for $f_{\text{Sig3}}(t)$, $f_{\text{Sig4}}(t)$ and $f_{\text{Sig5}}(t)$ are listed in Table 6. All computations are conducted on MATLAB R2020a on a PC with an Intel Xeon W-2123 CPU, 16.0 GB of RAM and 64-bit Windows
410 10. It can be seen that the EFD requires the shortest computation time among the six methods. The computation times associated with the EFD and EWT are comparable and while those of the FDM-HTL and FDM-LTW are large. The computational times of the VMD and EMD depended on their parameters; though they can greatly vary, they are longer than that of the
415 EFD. Hence, it can be concluded that the EFD is the most computationally efficient.

5. Concluding remarks

In this paper, an accurate and efficient EFD method is proposed to decompose time-domain signals. The EFD consists of two critical steps:
420 the improved segmentation technique and construction of a filter bank. In the improved segmentation technique, only meaningful Fourier spectrum

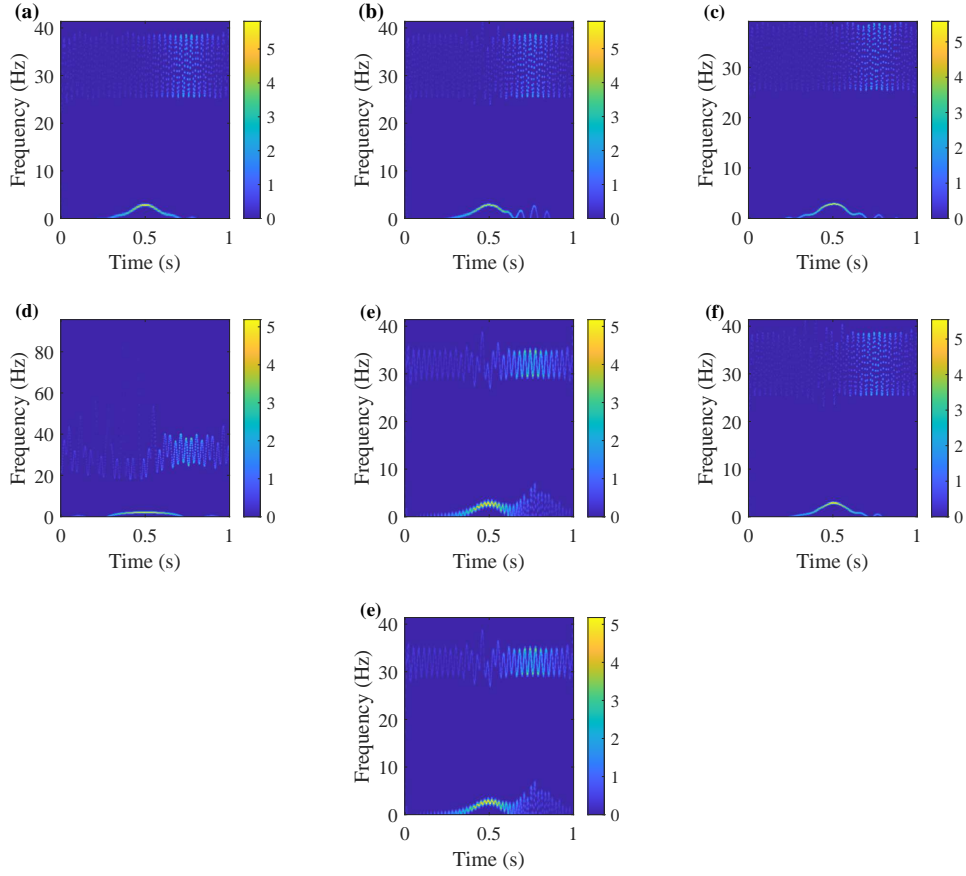


Figure 15: TFR results of $f_{\text{Sig}3}(t)$ by: (a) EFD, (b) EWT, (c) FDM-LTH, (d) FDM-HTL, (e) VMD, (f) EMD, and (g) benchmark.

Table 6: Computation time for $f_{\text{Sig}3}(t)$, $f_{\text{Sig}4}(t)$ and $f_{\text{Sig}5}(t)$ by the EFD, EWT, FDM-LTH, FDM-HTL, VMD and EMD.

Signal	Computation Time (s)					
	EFD	EWT	FDM-LTH	FDM-HTL	VMD	EMD
$f_{\text{Sig}3}(t)$	1.66×10^{-2}	6.33×10^{-2}	1.75×10^{-1}	1.09×10^{-1}	1.75×10^{-1}	8.21×10^{-2}
$f_{\text{Sig}4}(t)$	1.54×10^{-2}	6.61×10^{-2}	2.59×10^{-1}	1.04×10^{-1}	1.96×10^{-0}	9.58×10^{-2}
$f_{\text{Sig}5}(t)$	1.67×10^{-2}	7.02×10^{-2}	1.59×10^{-1}	1.16×10^{-1}	1.41×10^{-0}	1.51×10^0

components are included and the last segment that can contain noise is narrowed, which can decrease the size of the segment and alleviate adverse effects of noise. In a constructed filter bank, transition phases of filter
425 functions are eliminated, which can improve the decomposition performance for closely-spaced modes. Two numerical investigations are conducted on non-stationary signals, it is shown that the EFD can yield decomposition results with high accuracy and consistency. Two numerical investigations are conducted on two stationary signals to study the decomposition performance
430 of the EFD for closely-spaced modes. It is shown that the EFD can yield decomposition results for the closely-spaced modes with high accuracy and consistency and its decomposition results are more accurate than those by the other decomposition methods. In addition, it is shown that the EFD can yield accurate TFRs for non-stationary signals. Comparisons between
435 computation times by the EFD, EWT, FDM, VMD and EMD show that the EFD is the most computationally efficient. A future work can be an investigation of the applicability of the EFD to signals/data of higher dimensions, such as digital images.

A MATLAB implementation of the proposed algorithm will be available
440 at the MATLAB Central.

Acknowledgments

The author Y.F. Xu is grateful for the financial support from the National Science Foundation through Grant No. CMMI-1762917. The authors gratefully acknowledge valuable discussions with and input from Dr. Gang Yu, Dr.
445 Pushpendra Singh, Dr. Shiqian Chen and Dr. Heng Li. They also thank people who share their contributions to the signal processing community.

Conflicts of Interest

The authors declare no conflict of interest.

References

- 450 [1] A. Bhattacharyya, R. B. Pachori, A multivariate approach for patient-specific eeg seizure detection using empirical wavelet transform, *IEEE Transactions on Biomedical Engineering* 64 (9) (2017) 2003–2015.
- [2] F. Li, B. Zhang, S. Verma, K. J. Marfurt, Seismic signal denoising using thresholded variational mode decomposition, *Exploration Geophysics*
455 49 (4) (2018) 450–461.
- [3] J. Pan, J. Chen, Y. Zi, Y. Li, Z. He, Mono-component feature extraction for mechanical fault diagnosis using modified empirical wavelet transform via data-driven adaptive fourier spectrum segment, *Mechanical Systems and Signal Processing* 72 (2016) 160–183.
- 460 [4] S. Chen, Y. Yang, Z. Peng, X. Dong, W. Zhang, G. Meng, Adaptive chirp mode pursuit: Algorithm and applications, *Mechanical Systems and Signal Processing* 116 (2019) 566–584.
- [5] A. Upadhyay, R. Pachori, Speech enhancement based on memd-vmd method, *Electronics Letters* 53 (7) (2017) 502–504.
- 465 [6] D. Iatsenko, P. V. McClintock, A. Stefanovska, Nonlinear mode decomposition: a noise-robust, adaptive decomposition method, *Physical Review E* 92 (3) (2015) 032916.
- [7] N. E. Huang, Z. Shen, S. R. Long, M. C. Wu, H. H. Shih, Q. Zheng, N.-C. Yen, C. C. Tung, H. H. Liu, The empirical mode decomposition

- 470 and the hilbert spectrum for nonlinear and non-stationary time series
analysis, *Proceedings of the Royal Society of London. Series A:
mathematical, physical and engineering sciences* 454 (1971) (1998) 903–
995.
- [8] G. Rilling, P. Flandrin, P. Goncalves, et al., On empirical mode
475 decomposition and its algorithms, in: *IEEE-EURASIP workshop on
nonlinear signal and image processing*, Vol. 3, NSIP-03, Grado (I), 2003,
pp. 8–11.
- [9] R. Rato, M. D. Ortigueira, A. Batista, On the hht, its problems, and
some solutions, *Mechanical systems and signal processing* 22 (6) (2008)
480 1374–1394.
- [10] Z. Wu, N. E. Huang, Ensemble empirical mode decomposition: a noise-
assisted data analysis method, *Advances in adaptive data analysis* 1 (01)
(2009) 1–41.
- [11] M. E. Torres, M. A. Colominas, G. Schlotthauer, P. Flandrin, A
485 complete ensemble empirical mode decomposition with adaptive noise,
in: *2011 IEEE international conference on acoustics, speech and signal
processing (ICASSP)*, IEEE, 2011, pp. 4144–4147.
- [12] H. Li, Z. Li, W. Mo, A time varying filter approach for empirical mode
decomposition, *Signal Processing* 138 (2017) 146–158.
- 490 [13] K. Dragomiretskiy, D. Zosso, Variational mode decomposition, *IEEE
transactions on signal processing* 62 (3) (2013) 531–544.
- [14] S. McNeill, Decomposing a signal into short-time narrow-banded modes,
Journal of Sound and Vibration 373 (2016) 325–339.

- [15] S. Chen, X. Dong, Z. Peng, W. Zhang, G. Meng, Nonlinear chirp mode
495 decomposition: A variational method, *IEEE Transactions on Signal
Processing* 65 (22) (2017) 6024–6037.
- [16] J. Gilles, Empirical wavelet transform, *IEEE transactions on signal
processing* 61 (16) (2013) 3999–4010.
- [17] Z. Luo, T. Liu, S. Yan, M. Qian, Revised empirical wavelet transform
500 based on auto-regressive power spectrum and its application to the mode
decomposition of deployable structure, *Journal of Sound and Vibration*
431 (2018) 70–87.
- [18] Y. Xin, H. Hao, J. Li, Operational modal identification of structures
based on improved empirical wavelet transform, *Structural Control and*
505 *Health Monitoring* 26 (3) (2019) e2323.
- [19] J. P. Amezcua-Sanchez, H. Adeli, A new music-empirical wavelet
transform methodology for time–frequency analysis of noisy nonlinear
and non-stationary signals, *Digital Signal Processing* 45 (2015) 55–68.
- [20] P. Singh, S. D. Joshi, R. K. Patney, K. Saha, The fourier
510 decomposition method for nonlinear and non-stationary time series
analysis, *Proceedings of the Royal Society A: Mathematical, Physical
and Engineering Sciences* 473 (2199) (2017) 20160871.
- [21] R. W. S. Alan V. Oppenheim, *Discrete Time Signal Processing*, 3rd
Edition, Prentice Hall, 2009.
- 515 [22] I. Daubechies, *Ten lectures on wavelets*, SIAM, 1992.
- [23] J. Gilles, G. Tran, S. Osher, 2d empirical transforms. wavelets, ridgelets,

and curvelets revisited, *SIAM Journal on Imaging Sciences* 7 (1) (2014) 157–186.

[24] B. Picinbono, On instantaneous amplitude and phase of signals, *IEEE Transactions on signal processing* 45 (3) (1997) 552–560.

[25] F. J. Harris, *Multirate signal processing for communication systems*, Prentice Hall PTR, 2004.

[26] T. Y. Hou, Z. Shi, Adaptive data analysis via sparse time-frequency representation, *Advances in Adaptive Data Analysis* 3 (01n02) (2011) 1–28.

[27] G. Rilling, P. Flandrin, One or two frequencies? the empirical mode decomposition answers, *IEEE transactions on signal processing* 56 (1) (2007) 85–95.